Journal of Sound and Vibration 619 (2025) 119388

Contents lists available at ScienceDirect

Journal of Sound and Vibration

journal homepage: www.elsevier.com/locate/jsvi

Piezoelectric floating mass transducer as micro actuator working with magnetorheological elastomer

R. Rusinek [a], S. Lenci [b,*]

[a] *Lublin University of Technology, Department of Applied Mechanics, Lublin, Poland*
[b] *Polytechnic University of Marche, Department of Civil and Building Engineering, and Architecture, Ancona, Italy*

ARTICLE INFO

Keywords:
Piezoelectric floating mass transducer
Middle ear implant
Magnetorhelogical elastomer
Bouc–Wen hysteresis
Piezoelectric actuator

ABSTRACT

This study analyzes the application of a piezoelectric floating mass transducer (FMT) combined with a magnetorheological elastomer (MRE) for exciting the ossicular chain and general mechanical systems. The results highlight the effectiveness of the FMT in inducing vibrations, further enhanced by the adaptive properties of the MRE, making it a promising option for broader engineering and biomedical applications, including hearing restoration devices. The study confirms that resonance tuning and the magnetic field-dependent properties of the MRE are crucial for optimizing vibration performance, significantly affecting energy transfer, while the MRE provides additional control over stiffness and damping. Compared to conventional actuators, the FMT-MRE system offers advantages in terms of frequency adaptability, though challenges remain due to nonlinear behaviors induced by MRE hysteresis. The full practical implementation is limited by the occurrence of irregular vibrations and bistability under high-voltage excitations. Firstly, a simplified 1-degree-of-freedom pure MRE system modeled with the Bouc–Wen component is analyzed at low and high excitation frequency. Next, application for the middle ear implants is studied in case of linear and nonlinear system.

1. Introduction

The Floating Mass Transducer (FMT) converts electric signals into mechanical vibrations. The name of FMT usually refers to an active element of the middle ear implant and was introduced by MEDEL (wwww.medel.com). The FMT implanted in the human ear is about the size of a grain of rice [1–3]. Generally, there are two types of FMTs: electromagnetic and piezoelectric ones, but the classical and the most popular one is an electromagnetic device composed of a case, a magnet and a coil powered by AC voltage from a signal processing unit. Both the electromagnetic FMT, tested in worldwide literature [4–13] and the piezoelectric FMT (PFMT), studied in [14–22], suffers from the fact that the FMT can stimulate only one constant frequency of an object, commonly near to the natural frequency of the FMT or the system with FMT. However, the electromagnetic FMT suffers from the interference due to the environmental electromagnetic fields, unlike to PFMT. Therefore, PFMT is more and more promising and popular.

This paper describes a modified smartPFMT with changeable resonance frequency (not only the fixed one) that could stimulate a main system working at different frequencies. The new idea of SmartPFMT with variable natural frequency is based on a variable stiffness material (VSM) that support the floating mass. VSMs are a kind of smart materials, proposed for SmartPFMT, because they have the ability to change their properties in response to specific external stimuli, such as temperature, humidity, light, magnetic field, electromagnetic field or applied stress. Moreover, the materials can work both as actuators and sensors, which is a great advantage.

* Corresponding author.
E-mail address: lenci@univpm.it (S. Lenci).

https://doi.org/10.1016/j.jsv.2025.119388
Received 17 March 2025; Received in revised form 6 July 2025; Accepted 8 August 2025
Available online 29 August 2025
0022-460X/

Magnetorheological elastomer (MRE) is one of the VSM, that is chosen for FMT element responsible for stiffness change (and the natural frequency) because it needs short time to amend its properties. Therefore, it can be used in dynamical systems. Moreover, the smartPFMT can work as a sensor when activation of an object is not required or even harmful, e.g. in the middle ear implant when sleeping and noise is approaching to the ear or in other engineering applications where battery charging is more important than main system stimulation at the moment. Then, the smartPFMT could work as energy harvester with adjustable stiffness or/and damping properties. Application of MREs is still increasing, as observed by the increasing number of published works in this field. A simple search using the keyword "model of magnetorheological elastomer" in Lens.org has showed 2064 scholarly works and 156 citing patents since 2000.

MRE is a typical nonlinear viscoelastic material with field-dependent mechanical properties, i.e. stiffness and damping. Modeling of the complex behavior of MREs is an essential step towards its engineering applications [23]. Generally, two kinds of MRE models have been developed: microstructure-based (micromechanical) and phenomenological ones. The micromechanical models consider the interaction between micrometer-sized magnetic particles within the elastomeric medium considering different lattice configurations [24–27]. The majority of micromechanical models are based on hyperelastic assumptions. Many of them were conducted in order to develop models to predict the response behavior of MREs under static or low-frequency (quasi-static) conditions. These models, however, could not capture the nonlinear hysteresis behavior of MREs and their response behavior under a wide range of frequency and magnetic field. This is mainly due to the viscoelastic nature of MREs which should be considered to evaluate their dynamic performance [27]. Therefore, a phenomenological models is applied in this study. Most of these models use classical rheological circuits composed of springs, Newtonian dashpots, and other elements representing response delays connected in different ways. Some models of MREs take into account viscoelastic behavior based on a fractional derivative model. In this regard, the most common combination of a spring and a fractional derivative element (Abel dashpot) is presented in [28–30]. The components involved in this combination can be modified to yield other possibilities [31–34].

The development of a higher-order fractional derivative model can be achieved by combining a fractional Maxwell model with a fractional Kelvin model in parallel. It is noted that the fractional Maxwell model is found to be different in describing both MREs' shear storage and shear loss module compared with the two-Maxwell model which comprised two-integer-order Maxwell chains [34]. A comparison of the efficiency of six different models, that is: Maxwell, Kelvin–Voigt, Zener, generalized Kelvin–Voigt, hybrid Maxwell–Kelvin–Voigt and generalized Maxwell model, is presented in [32]. Some MRE models have been developed to describe MRE behavior in a particular application. In this regard, a classical model of nonlinear hysteresis, the Bouc–Wen model, can be effectively used [27,35]. By modifying the conventional Bouc–Wen model, Behrooz et al. [36] have proposed a new model for a specified loading condition. Another model with hysteresis is developed by Eem et al. [37], that is based on the Ramberg–Osgood model originally introduced in 1943. Eem et al. have connected the Ramberg–Osgood model with the Maxwell one. Next, Vatandoost et al. [38] have introduced a new phenomenological model for studying the dynamic behavior of MREs under coupled tension–compression mode.

Each model has some advantages and disadvantages. A promising method for reducing the existing drawbacks of each model is to combine different approaches. The combination of continuum approach and the microstructure approach has been used in some studies. Such modeling can somehow obtain the benefits of microstructure modeling (high accuracy) and continuum-based method (relatively lower computational time) simultaneously [27].

1.1. Motivation and aim

Generally, lumped parameters models of the PFMT are known in the literature, as well as the model of MRE. However, the new idea of connecting both elements in order to develop a smartPFMT that can change its characteristic for using with different mechanical systems is developed.

1.2. Novelty

To overcome shortcomings with constant resonance frequency of a FMT, reported in Introduction, an improved solution of the transducer with MRE is proposed here. Although, models of a FMT and a MRE are described in numerous number of publications, models of FMT with MRE are hard to find. Therefore, this is a first attempt to study such a system.

1.3. Paper layout

The paper is organized as follows, in Section 2 the model of the piezoelectric floating mass transducer with magnetorheological elastomer (smartFMT) is described. Section 3 is devoted to linear vibrations of simplified model. Next, in Section 4 the numerical analysis of the smartFMT as a actuator and a sensor is presented. Finally, conclusions are presented in Section 5.

2. Model of smartFMT

The piezoelectric floating mass transducer with magnetorheological elastomer (smartFMT) is modeled here as a three degree-of-freedom (3dof) system (described by the three coordinates, x_s, x_1 and x_2), as schematically illustrated in Fig. 1. The transducer is fixed to the main system (M_S), also known as 'body', by means of the MRE, that is a key element and is assumed to be massless, since its mass is negligible with respect to the others (this is why the same F_{MRE} is applied on both sides of the MRE elastomer). Both the MRE and the transducer are described separately in the following subsections.

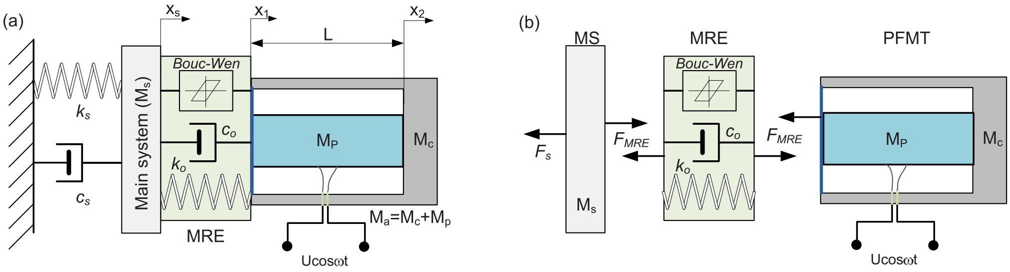

Fig. 1. (a) Model of smartFMT and (b) free body diagram of smartFMT.

Table 1
Value for field-dependent MRE parameters after [35].

Parameter	Value	Unit
A_a	0.80225	–
A_b	1.5043	A^{-1}
α_a	0.15371	–
α_b	0.28939	A^{-1}
k_{0a}	1.3103/5	N/mm
k_{0b}	3.322/5	N/(A mm)
c_{0a}	0.044604/4000	N s/mm
c_{0b}	0.087104/4000	N s/(A mm)
β	0.3	mm^{-1}
γ	−0.6	mm^{-1}

2.1. Magnetorheological elastomer

In MRE modeling, the most important challenge is the nonlinear relationship between force and speed. To accurately describe these unique behaviors of the MRE, the phenomenological model proposed by Yang et al. [35] is used. It is based on a Bouc–Wen component, which reproduces hysteresis loops, in parallel with a Kelvin–Voigt element, as shown schematically on Fig. 1. The Bouc–Wen component is described by the evolutionary variable z that represents a function of the time history of the displacement. The force generated by the MRE (F_{MRE}) is given by

$$F_{MRE} = \alpha k_0(x_1 - x_s) + (1-\alpha)k_0 z + c_0(\dot{x}_1 - \dot{x}_s), \tag{1}$$

where the evolutionary variable z is described as

$$\dot{z} = A(\dot{x}_1 - \dot{x}_s) - \beta|(\dot{x}_1 - \dot{x}_s)||z|^{n-1}z - \gamma(\dot{x}_1 - \dot{x}_s)|z|^n. \tag{2}$$

Stiffness and viscous damping coefficient of the MRE are represented by k_0 and c_0, respectively. The linear part of F_{MRE} is $\alpha k_0(x_1-x_s)+c_0(\dot{x}_1-\dot{x}_s)$, while the purely hysteretic component is defined as $(1-\alpha)k_0 z$ in which $\alpha \in (0,1)$. A, n, β, γ are nondimensional parameters responsible for the shape and the size of the hysteresis loops. Different combinations of the signs of $\beta+\gamma$ and $\beta-\gamma$ reproduce different shapes of hysteresis loops, as shown in [39].

2.2. Field-dependent MRE model

The presented model of the MRE is valid when the current is constant. However, in case of smartFMT a versatile model is expected also to describe the mechanical behavior when the magnetic field is varied in time to change a natural frequency of the system. To this end, a study on the field-dependent parameters is proposed after [35], according to following linear expressions

$$A = A_a + A_b I, \quad \alpha = \alpha_a + \alpha_b I, \quad k_0 = k_{0a} + k_{0b} I, \quad c_0 = c_{0a} + c_{0b} I. \tag{3}$$

Parameters of the MRE (from [35]), tailored for the micro-size PFMT, are collected in Table 1. Thus, the MRE should be put inside a variable magnetic field produced by a coil on a core, that is schematically presented in Fig. 2. A ferromagnetic U-shaped core channels the magnetic flux efficiently, reducing losses and focusing the field through the MRE. A copper coil is wound around one leg of the core and connected to a DC power supply. When current flows through the coil, it generates a magnetic field (per Ampère's Law). The magnetic field circulates through the core, across the air gap containing the MRE, and back through the core. This ensures the MRE is exposed to a strong, uniform field. The MRE contains ferromagnetic particles embedded in a soft elastomer. Under the influence of the magnetic field. The particles align, increasing the stiffness of the material. The internal friction also increases, enhancing damping. By adjusting the current in the coil, the strength of the magnetic field can be precisely controlled—tuning the mechanical response of the FMT or other MRE-integrated device in real time.

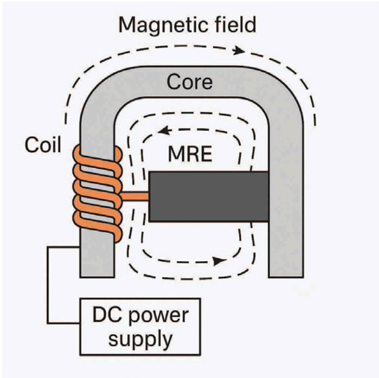

Fig. 2. Schematic view of magnetic circuit configuration for the MRE implementation.

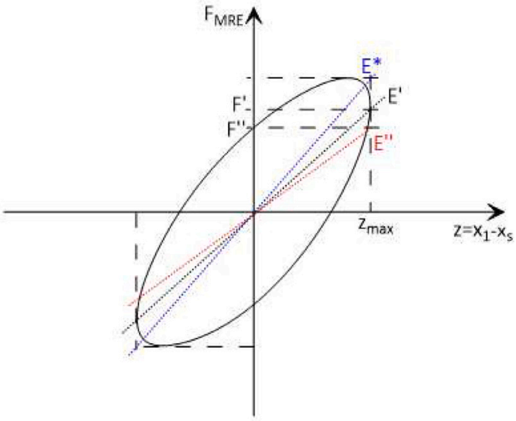

Fig. 3. Hysteresis of MRE with storage, loss and equivalent young modulus.

2.3. Hysteresis effect

Hysteresis of MREs is describe here by the Bouc–Wen model (see Section 2.1) which represents the flow and deformation of materials as a response to an applied stress or strain. The elastic component of a material's response is defined as a storage modulus (E'), while a loss modulus (E'') represents the viscous component of a material's response. E' indicates the material's ability to store energy when subjected to deformation and then release it when the stress is removed. A higher storage modulus implies a stiffer material that can store more elastic energy. On the other hand, E'' indicates the material's ability to dissipate energy as heat when subjected to deformation. A higher loss modulus implies a more viscous material that dissipates more energy. Graphically, the storage and loss modulus are presented in Fig. 3 together with the equivalent (complex) Young's Modulus defined as

$$E^* = E' + iE'', \quad |E^*| = \sqrt{(E')^2 + (E'')^2}. \tag{4}$$

The storage and loss modulus can be calculated as

$$E' = F'/z_{max}, \quad E'' = F''/z_{max}. \tag{5}$$

F' means the MRE force at z_{max}, while F'' is the force at $z = 0$. Next, a loss factor (η) can be expressed as

$$\eta = E''/E'. \tag{6}$$

However, loss factor (η) is not accurate enough to describe energy loss (EL) that is proportional to a hysteresis area. The area of hysteresis loop, presented in Fig. 3, can be calculated to estimate EL factor. The change in the shape of the MRE hysteresis loop under the influence of different forcing conditions will be analyzed in the following sections.

2.4. Piezoelectric floating mass transducer

Generally, the PFMT is composed of a multilayered piezoelectric element (M_p) and a metal case (M_c), schematically presented in Fig. 1b. The total mass of the PFMT is $M_a = M_p + M_c$.

The PFMT can stimulate the M_s or can be stimulated by the M_s. The expansion and contraction of the piezoelectric actuator from an applied voltage signal causes vibration to be transferred to the MS by the law of action-and-reaction. Usually, piezoelectric element is made of a multilayered PZT [19] or sometimes of the multilayered PMN-PT [20,40]. Generally, PMN-PT has high dielectric, high piezoelectric constants and large electromechanical coupling factor. In the low frequency regime, the performances are much higher than the best PZT ceramics because of their high piezoelectric constants that reach five times those of the best PZT ceramics [41].

In a multilayered actuator, the elongation ΔT of the piezoelectric material in the absence of any restraint is given by

$$\Delta T = n d_{33} U(t), \tag{7}$$

where n is the number of layers, d_{33} the coefficient of the piezo-constitutive law relating strain and voltage, $U(t)$ is the applied voltage. When a force F_{MRE} is applied to the PFMT (from the main system thought the MRE, see Fig. 1b), the relative displacement between the left and the right side of the PFMT is given by following equation

$$\Delta x_e = x_1 - x_s = \frac{F_{MRE}}{k_p}, \tag{8}$$

where $k_p = EA/L$ is the axial stiffness of the PFMT. Summing up, the relative total displacement between the left and right sides of the PFMT, caused by the voltage and the force F_{MRE} is given by

$$\Delta x = x_2 - x_1 = \Delta T + \Delta x_e = n d_{33} U(t) + \frac{F_{MRE}}{k_p}. \tag{9}$$

Note, that the transverse strain (d_{31} - d_{32}) is neglected because the model of MRE actuator is one dimensional. Moreover, the longitudinal direction is the most important to excite motion. In literature, there are both simulation and experimental studies that support the simplification of using only the longitudinal piezoelectric constant in specific modeling scenarios [42–44]. This approach is particularly valid when the piezoelectric material is polarized in the thickness direction and the electric field is aligned accordingly, such that the primary deformation and energy conversion are dominated by the mode.

2.5. System with smartPFMT

The smartPFMT is used here to excite motion of the main system. The equations of motion of the smartPFMT system can be immediately obtained by the Newton law applied to the free body diagram of Fig. 1b, and are

$$\begin{aligned} &M_s \ddot{x}_s + k_s x_s + c_s \dot{x}_s - F_{MRE} = 0, \\ &M_a \ddot{x}_2 + F_{MRE} = 0. \end{aligned} \tag{10}$$

In the second equation it is neglected the different position of the center of mass of the transducer due to the elongation of the piezoelectric material, which is reasonable when $M_c \gg M_p$. It is worth to remind that there is no equation of motion for the RME since its mass has been neglected.

From the previous considerations it follows that the model of the smartPFMT is given by the Eqs. (1), (2), (9) and (10), that are reported all together for the reader benefit:

$$\begin{aligned} &M_s \ddot{x}_s + k_s x_s + c_s \dot{x}_s - F_{MRE} = 0, \\ &M_a \ddot{x}_2 + F_{MRE} = 0, \\ &\dot{z} = A(\dot{x}_1 - \dot{x}_s) - \beta |(\dot{x}_1 - \dot{x}_s)| |z|^{n-1} z - \gamma (\dot{x}_1 - \dot{x}_s) |z|^n, \\ &F_{MRE} = \alpha k_0 (x_1 - x_s) + (1-\alpha) k_0 z + c_0 (\dot{x}_1 - \dot{x}_s), \\ &x_2 - x_1 = n d_{33} U(t) + \frac{F_{MRE}}{k_p}. \end{aligned} \tag{11}$$

They are a system of 3 differential equations (the first three, where the first two of the second order, the third of the first order) and 2 algebraic equations (the last two), in the 5 unknowns x_s, x_2, z, x_1 and F_{MRE}. They will be solved in the following section with parameters typical for the middle ear application, that are presented in Table 2, where the main system represents 1dof middle ear model. Mass of the main system (M_s) is a typical one of ossicular chain consisted of the malleus, the incus and the stapes. Stiffness and damping (k_s, c_s) are selected so that the natural frequency of the system matches the first resonance frequency of the middle ear, while maintaining consistency in the vibration amplitudes of both systems (see e.g. [13]). Stiffness of piezoelement (k_p) used in middle ear implant is taken from [22], after [14].

3. Simplified 1dof MRE system

At the beginning, a simplified 1dof system with MRE, but without piezoelement is studied. In the system the field dependent MRE is analyzed to explore its dynamic behavior in low and high frequency regions. This 1dof MRE model is presented in Fig. 4. Since the simplified system has not a piezoelement, motion of the mass (M_a) is excited by a harmonic force $P_o \cos(\omega t)$ directly applied to it, where $P_o = 0.4$ N is taken as the reference value. Assuming that the system can be used for an implantable middle ear hearing device, micro mass is taken into consideration with parameters specified in Table 2 where field dependent MRE parameters defined by Eq. (3) are presented in Table 1.

Table 2
Mechanical and electrical parameters of the smartPFMT and main system.

Parameter	Value	Unit
M_s	54.78	mg
$M_a = M_p + M_c$	10	mg
k_p	11.2×10^7	N/mm
k_s	2.1626	N/mm
c_s	0.6366	N s/m
U_0	4	mV
d_{33}	1×10^{-8}	–
n	100	

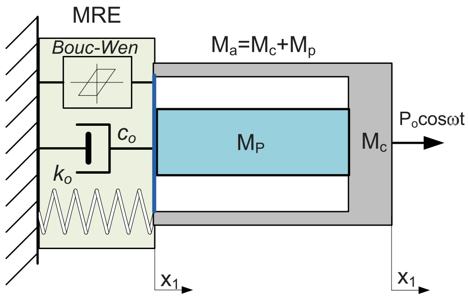

Fig. 4. Simplified 1dof model with MRE (1dof MRE).

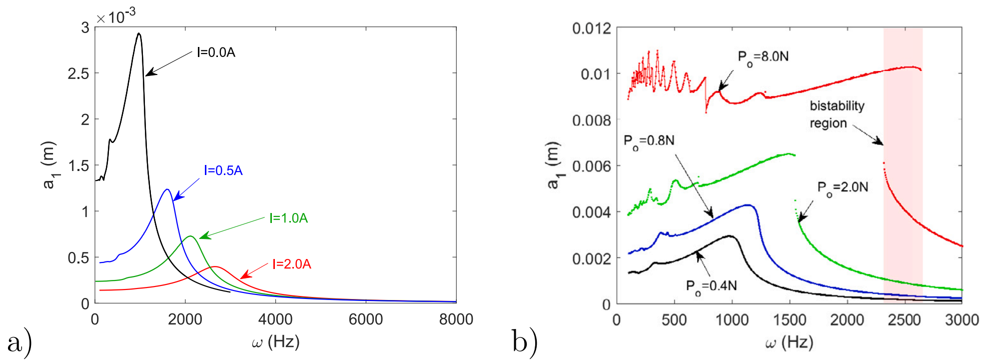

Fig. 5. Amplitude (a_1) of the 1dof MRE system versus excitation frequency (ω); (a) excited by harmonic force ($P_o = 0.4$ N) for different current I, (b) forced by different P_0 for current $I = 0$ A. (For interpretation of the references to color in this figure, the reader is referred to the web version of this article.)

3.1. Resonances

One of the most important features of the MRE system is its ability to alter the resonant frequency under the influence of a magnetic field. A resonance can be shifted toward the right when current is increased, for instance from 975 Hz at $I = 0$ A to 2670 Hz at $I = 2$ A (Fig. 5a). However, the increase in current also causes a decrease in the peak of vibration amplitude from 2.93 mm to 0.4 mm. It is produced by current-induced simultaneous increase in stiffness and damping of the system. As the excitation amplitude (P_o) increase (see Fig. 5b), the system amplitude increases and the nonlinear effect i.e. the hardening of the frequency response curve, becomes more and more evident, up to bistability. This phenomenon, marked in pink color in Fig. 5b ($P_o = 8$ N), is due to nonlinear properties of the Bouc–Wen model of hysteresis. For $P_o > 2$ N the system has two stable periodic solutions and one unstable. This multiplicity of the stable solutions can be unwanted in practical applications. More information about resonances can be drawn from resonance maps depicted in Fig. 6. Note, that when the system has two solutions in the bistable region, then Fig. 6 shows the bigger one (maximal).

There is another adverse effect of instability, observed on the left-hand side of the resonance curve (Figs. 6a and 5b) especially in the case of stronger excitation ($P_0 = 10-20$ N) and low frequency range ($\omega < 1$ kHz). This region is suspected of quasi-periodic or poly-harmonic vibration. Interestingly, that amplitude (a_1) is high (resonance) at low current (I) only if $\omega < 2.5$ kHz (Fig. 6b). Next, for a higher ω, amplitude jump-down is possible. This phenomenon is also observed in Fig. 5b as a bistable effect when excitation frequency (ω) increases and decreases.

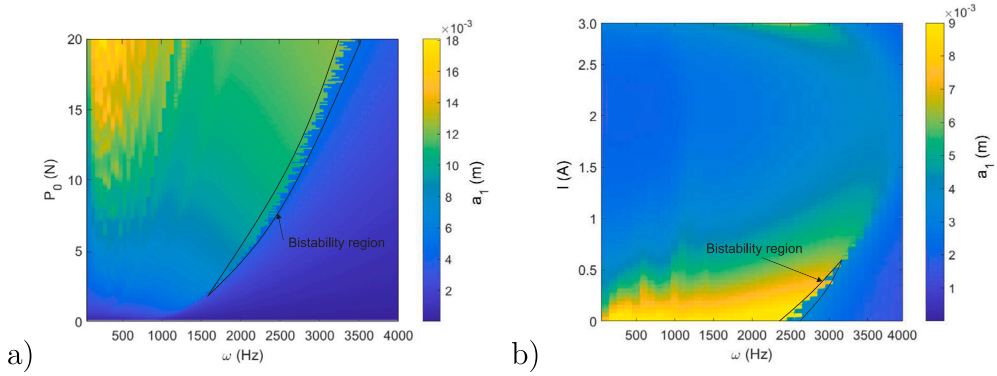

Fig. 6. Maximum of a_1 in the 1dof MRE system versus excitation frequency (ω) and (a) excitation amplitude P_0, (b) current I. Panel (a) is made for $I = 0$ A while (b) for $P_0 = 8.0$ N.

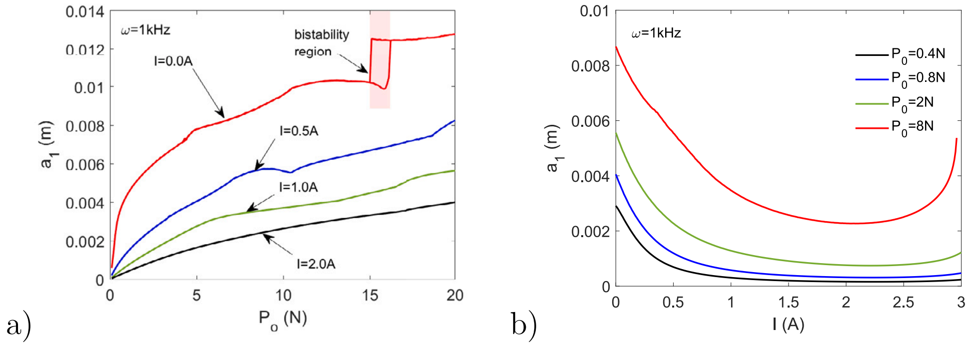

Fig. 7. Amplitude (a_1) in the 1dof MRE system versus an excitation amplitude P_0 (a) and current I (b), for excitation frequency ($\omega = 1$ kHz).

The amplitude curves for $\omega = 1$ kHz are presented in Fig. 7 as an example of frequency typical for the middle ear implants. A bistability region induced by high excitation ($P_0 \approx 15$ N) is observed only for $I = 0$ A (Fig. 7a). The minimum vibration amplitude (a_1) is at $I = 2$ A. Generally, the higher the current, the lower the vibration amplitude. An increase of the current above $I = 1$ A practically does not change the amplitude (a_1) as presented in Fig. 7b. However, an increase in current beyond 3 A results in a loss of system stability, particularly under strong excitation $P_0 = 8$ N.

3.2. Harmonic and other vibration

The dynamics of this system are sensitive to excitation and current. The 1dof MRE system exhibits not only harmonic solutions but others that should be identified. To get this result, voltage and current are chosen as control parameters. Fig. 8 presents solutions maps generated on these parameters and excitation frequency (ω), where harmonic (H) period T (1T) solution (1S - only one solution) is revealed (H-1T-1S). Moreover, regions of two harmonic solutions (H-1T-2S), poly-harmonic one (PH-1S), quasi-harmonic two-solutions (QH-2S) and small regions of more than two quasi-periodic ones (QP-2moreS) are identified. Basically, poly-harmonic and quasi-harmonic vibration appear at low excitation frequency (ω), but the frequency border increases with the rise in excitation amplitude (P_0).

An influence of current (I) at excitation $P_0 = 8$ N on system dynamics is shown in Fig. 8b. It can be seen that poly-harmonic vibration (PH-1S) can appear for low excitation ($\omega < 1.5$ kHz) and also at high frequency ($\omega > 3$ kHz) but only in a limited area. To gain deeper insight into the system's dynamics, phase space diagrams with red Poincaré points for selected solutions (from Fig. 8a) are depicted in Fig. 9. Thus, poly-harmonic motion (PH) with the period of 1T (relative to the excitation period) is presented in Fig. 9a, harmonic 1T motion (H-1T) in Fig. 9b and quasi-harmonic one (QH) in Fig. 9c. Moreover, for some parameters, there are two or more solutions (2S, 2moreS).

3.3. Low and high frequency hysteresis

The excitation frequency (ω) is another key parameter that influences the hysteresis shape. Usually MRE works in a low frequency system ($\omega < 10$ Hz) but here an application also for high frequency is tested to complement the analysis and check that possibility.

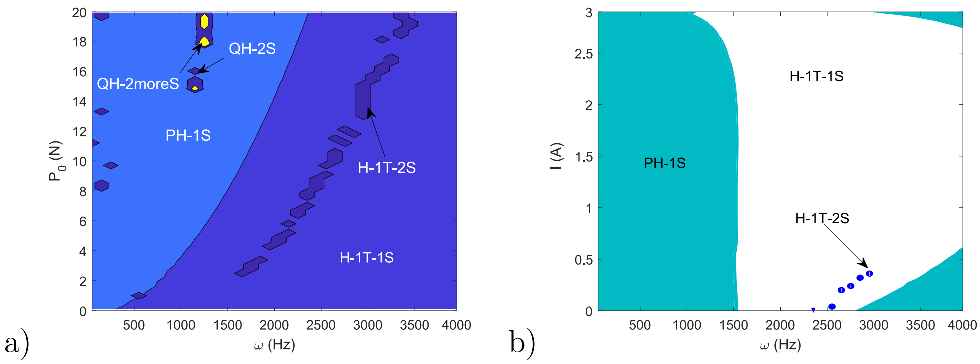

Fig. 8. Influence of excitation amplitude P_0 (a) and current I (b) on harmonic solutions in 1dof MRE system. The map are made for I = 0 A (a) and P_0 = 8.0 N (b). (For interpretation of the references to color in this figure, the reader is referred to the web version of this article.)

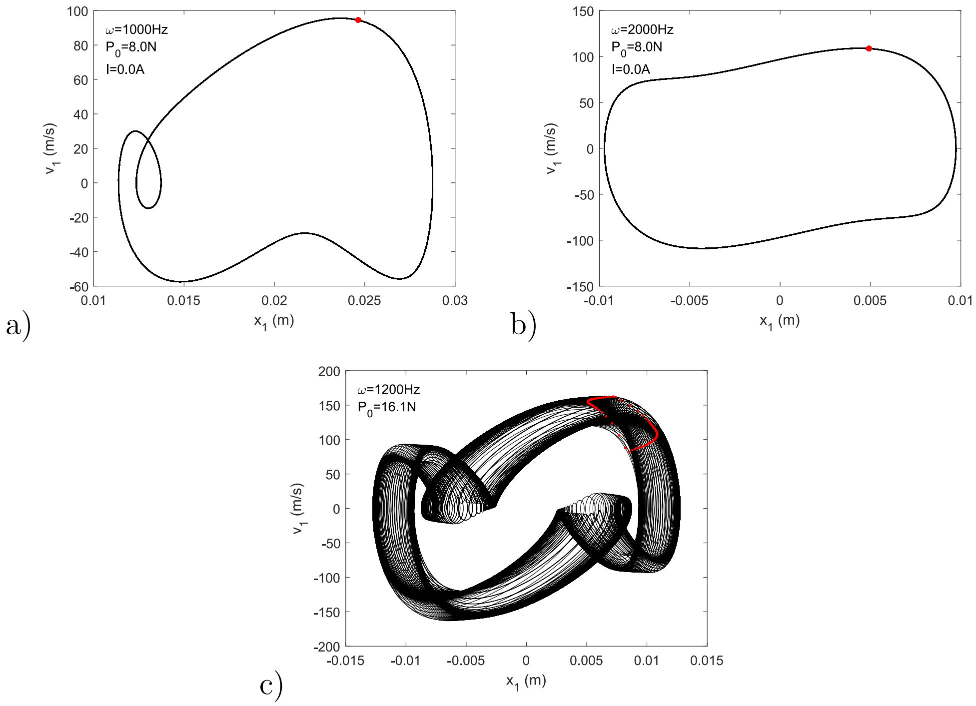

Fig. 9. Phase space diagrams with red Poincaré points for poly-harmonic (PH-1S) motion (a), harmonic (H-1T-1S) solution (b) and quasi-harmonic (QH) motion (c). (For interpretation of the references to color in this figure, the reader is referred to the web version of this article.)

When a low-frequency excitation (ω = 5 Hz) is applied, the hysteresis loops are illustrated in Fig. 10. By increasing the current, the storage modulus E' (i.e., the average slope of the hysteresis curves, which corresponds to the stiffness) of the MRE is increased and the loss modulus E'' (i.e. the area inside the loop, that corresponds to the loss energy) is decreased. However, a stronger excitation amplitude (P_o) causes the growth of the loss modulus (E'') and consequently the loss of energy efficiency.

For high frequency excitation (ω = 1 kHz) the system behavior at P_o = 0.4 N and P_o = 2.0 N (Fig. 11a-b) is similar but the narrowing of the hysteresis loop is observed with increasing excitation. Moreover, in case of P_o = 8.0 N (Fig. 11c), hysteresis is narrower as well, disturbed and shifted depending on the current. Energy loss factor versus excitation amplitude (P_0) is presented in Fig. 12. As expected, energy loss is higher when amplitudes are large and for small values of current (I). Moreover, an effect of energy hysteresis appears (red curve) when system bistability is observed.

The changes of the hysteresis loops due to the excitation frequency are illustrated in Fig. 13. Interestingly, the hysteresis is initially (ω = 5–10 Hz) smooth, assumes a (disturbed) saw-tooth shape for increasing ω, and then comes back to an almost regular behavior for very large frequencies (ω = 1 kHz).

The performed analysis confirms that the considered MRE model is rich enough in various nonlinear behaviors and can be used in different practical applications, but the nonlinear behaviors should be explained, understood and then possibly exploited.

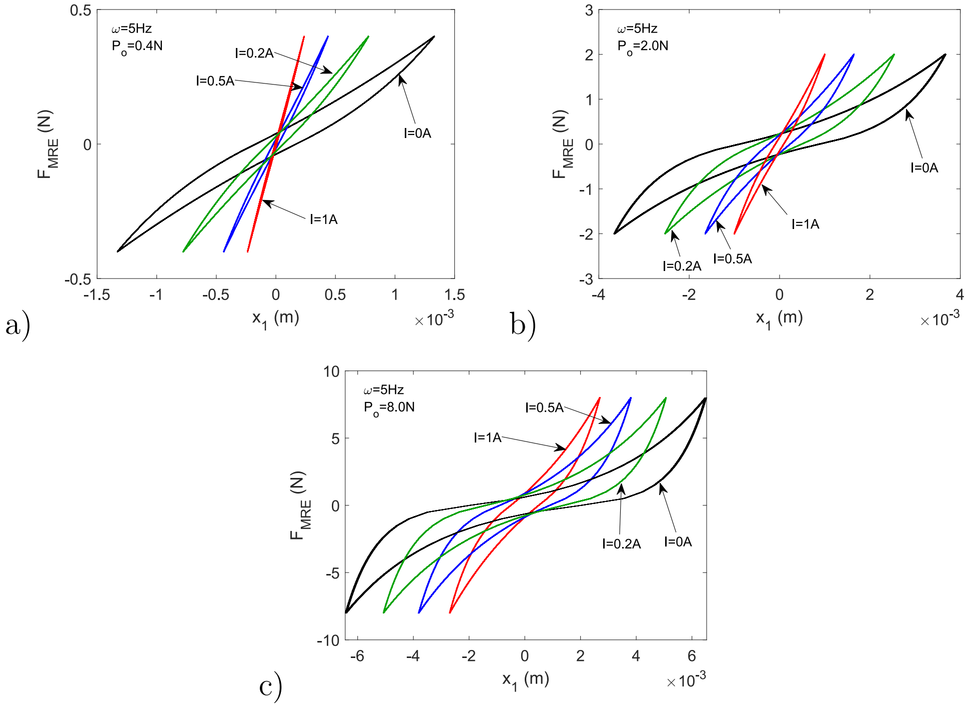

Fig. 10. Low frequency (ω = 5 Hz) hysteresis of the 1dof MRE system for different current (I) of MRE and excitation amplitude P_o = 0.4 N (a), P_o = 2.0 N (b), P_o = 8.0 N (a).

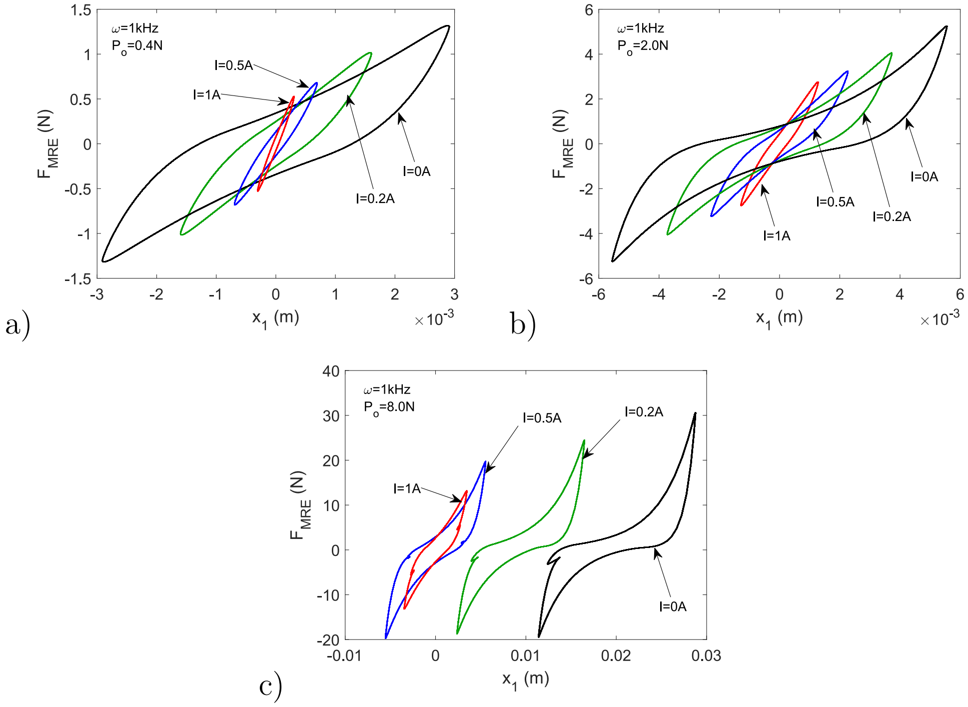

Fig. 11. High frequency (ω = 1 kHz) hysteresis of the 1dof MRE system for different current (I) and excitation amplitude P_o = 0.4 N (a), P_o = 2.0 N (b), P_o = 8.0 N (a).

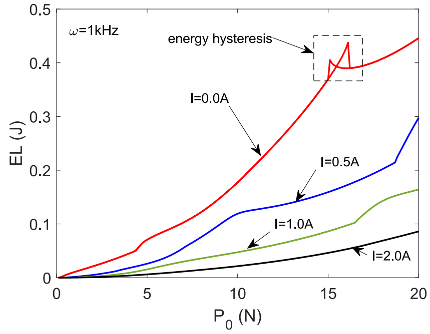

Fig. 12. Energy loss factor (EL) in the 1dof MRE system versus excitation amplitude P_0 for different current (I) and excitation frequency ω = 1 kHz. (For interpretation of the references to color in this figure, the reader is referred to the web version of this article.)

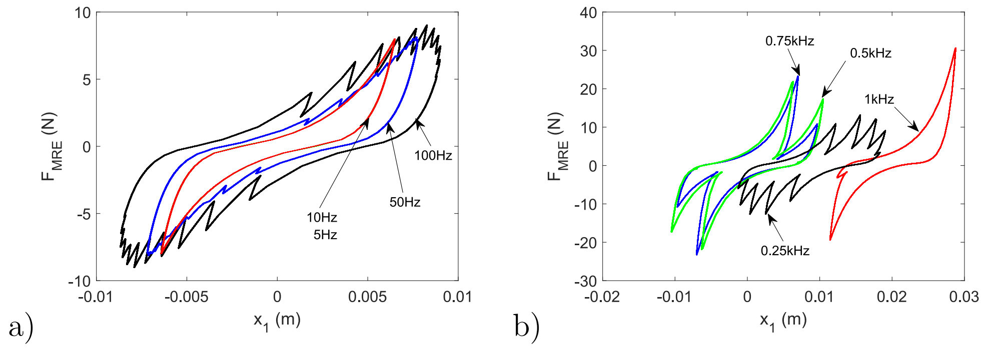

Fig. 13. Hysteresis for low frequency excitation ω = 5–100 Hz (a) and high frequency excitation ω = 100–1000 Hz (b) at excitation amplitude P_o = 8.0 N.

3.4. Damping and energy loss effect

Looking at resonance curves (Fig. 5a) and hysteresis loops presented in Figs. 10 and 11, some clarification concerning current (I) influence can be drawn. First of all, the resonance curves (Fig. 5a) suggest that increasing I, the hysteresis loops should be wider and energy loss higher because of the lower and wider resonance peak. However, the hysteresis loops become narrower and smaller (Figs. 10 and 11) both for low and high frequencies. This, a bit strange observation, is caused by changing field-dependent MRE parameters given by Eq. (3). On the one hand, c_0 and A increase damping with the current (I) producing smaller vibration amplitude and wider peak of the resonance curve. On the other hand, an increase of α (with current I), reduces the influence of the evolutionary variable z. This entails, energy loss calculated from hysteresis gets smaller with current (I) while damping raises at the same time. This effect is graphically presented in Fig. 14, where panel (a) shows evolutionary component $(1-\alpha)k_0 z$ on the left hand side (solid line), and damping component $c_0\dot{x}_1$ on the right as dashed lines. Moreover, energy loss (EL) calculated as a hysteresis area is presented in panel (b) which shows that energy loss and hysteresis width are the highest near resonance. The same conclusions can be drawn analyzing energy loss (EL) diagram presented in Fig. 15, where the influence of excitation frequency (ω), current (I) and excitation amplitude (P_0) is presented in panel (a) and (b), respectively.

4. Middle ear application of smartPFMT

The smartPFMT microsystem studied here can be applied for excitation of the middle ear when placed on the ossicular structure (usually in the long process of the incus, see [3,14,19,20,45]). Therefore, the smartPFMT is attached to the main 1dof system (M_s) which represents the ossicular chain (the malleus, the incus and the stapes) of the middle ear (Fig. 1). Parameters of the middle ear model (M_s, k_s and c_s), shown in Table 2, are assumed in such a way to get the main resonance of the middle ear model near 1 kHz, according to results reported in many papers devoted to middle ear dynamics [13,19,46–49]. Moreover, 1 kHz resonance for the middle ear is also promoted by the ASTM standard no F2504-05. The resonance peak is about 16 nm at 90 dB of sound pressure level [49]. To get similar vibration excited by smartPFMT a voltage $U = 0.004$ V is applied.

4.1. Vibration of linear system

Simplifying nonlinear Eq. (11) by assuming that $\alpha = 1$, the evolutionary variable (z) is redundant. Then, the magnetorheological force F_{MRE} is purely linear, and is given by

$$F_{MRE} = k_0(x_1 - x_s) + c_0(\dot{x}_1 - \dot{x}_s). \tag{12}$$

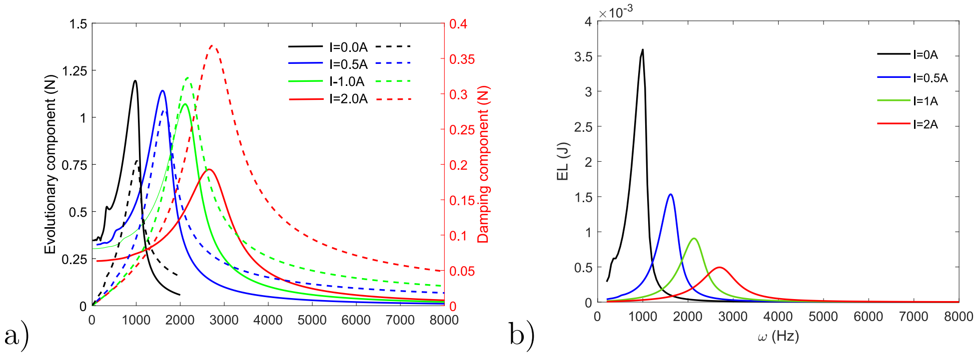

Fig. 14. Influence of charge (I) on evolutionary component z and damping component (a). Energy Loss (b) at excitation amplitude P_o = 8.0 N.

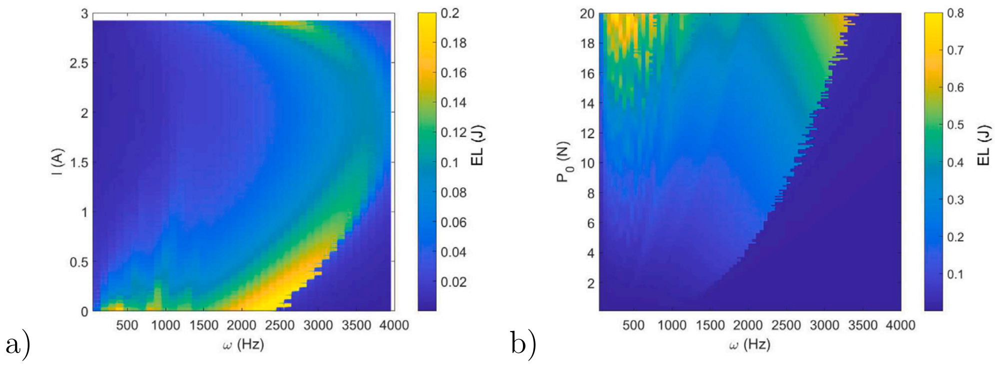

Fig. 15. Map of energy loss versus: current I for excitation amplitude P_0 = 8.0N (a), excitation amplitude P_0 at I = 0 A.

Thus, the differential equations of motion for the simplified model can be written as

$$\begin{aligned}
&M_s\ddot{x}_s + k_s x_s + c_s\dot{x}_s - F_{MRE} = 0,\\
&M_a\ddot{x}_2 + F_{MRE} = 0,\\
&F_{MRE} = k_0(x_1 - x_s) + c_0(\dot{x}_1 - \dot{x}_s),\\
&x_2 - x_1 = nd_{33}U(t) + \frac{F_{MRE}}{k_p}.
\end{aligned} \tag{13}$$

To find natural frequency of the linear (simplified) system, the eigenvalue problem is solved, neglecting the damping and external actions. The equations of motion Eq. (13) can be presented in a matrix form, where the inertia and stiffness matrix are

$$M = \begin{bmatrix} M_s & 0 \\ 0 & M_a \end{bmatrix}, \quad K = \begin{bmatrix} k_s + \frac{k_0}{1+k} & -\frac{k_0}{1+k} \\ -\frac{k_0}{1+k} & \frac{k_0}{1+k} \end{bmatrix}. \tag{14}$$

Since, $k = \frac{k_0}{k_p} \ll 1$, the stiffness matrix from Eq. (14) can be simplified to the following form

$$K = \begin{bmatrix} k_s + k_0 & -k_0 \\ -k_0 & k_0 \end{bmatrix}. \tag{15}$$

Then, the natural frequencies are

$$\omega_{01,02}^2 = \frac{M_a(k_0 + k_s) + M_s k_0 \pm \sqrt{[M_a(k_0 + k_s) + M_s k_0]^2 - 4M_a M_s k_0 k_s}}{2M_a M_s}. \tag{16}$$

The electrical current (I) is the main control parameter, since it changes the MRE stiffness (k_0, see Eq. (3)) and then the natural frequency of the system. This dependence is presented in Fig. 16a. The higher the current, the bigger the first (ω_{01}) and the second natural frequency (ω_{02}), but an increase of ω_{01} is much smaller (from 0.73 kHz to 0.9 kHz at I = 1.5 A, next it is almost constant) than ω_{02}, which increases from 1.12 kHz to 2 kHz at I = 1.5 A and even to 3.3 kHz at I = 3.0 A. Thus, the current is quite good as control parameter for ω_{02}. Natural frequency of the system can be adjusted by changing the actuator mass (M_a), too, as shown in Fig. 16b. The smaller the actuator mass, the higher the natural frequencies (ω_{01} and ω_{02}).

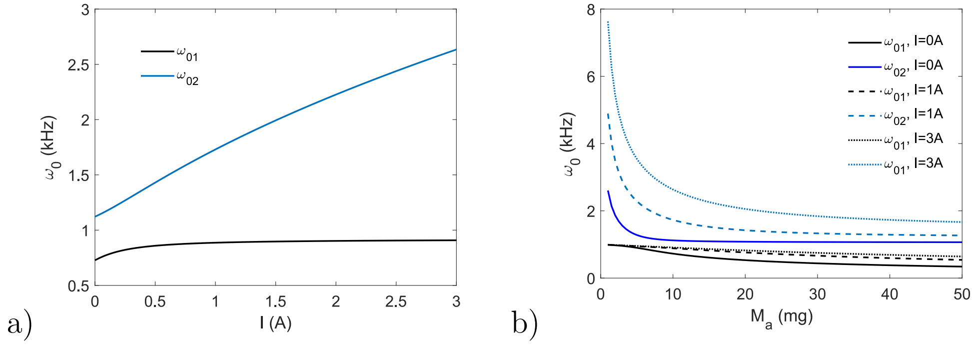

Fig. 16. Dependence of natural frequencies (ω_{01} and ω_{02}) of linear smartPFMT versus (a) electrical current (I) and (b) actuator mass (M_a).

4.2. Nonlinear system response

Interestingly, in the case of a nonlinear system with hysteresis, defined by the Bouc–Wen model and governed by Eq. (11), the resonance frequency (Fig. 17) depends on the current in different way, compared to the linear system (Fig. 16a). The peak amplitude A_s increases with the current for $I < 1$ A (Fig. 17a), next decreases ($I > 1$ A), while A_1 and A_2 always decrease (Fig. 17b–c). This behavior is not observed in the 1dof MRE system (Fig. 5a), where the highest peak amplitude A_s is at $I = 0$ A and then decreases with current I. The higher current causes the resonance curves to widen, resulting in a stronger damping in the system. This behavior is also consistent with 1dof MRE system presented in Fig. 5a. Moreover, in the nonlinear system, only one resonance is observed in Fig. 17. However, in both cases (linear and nonlinear) the resonance frequencies increase with the current (I), therefore this behavior is the same, but the linear undamped system has two natural frequencies that are not visible for the nonlinear and damped system. This phenomenon is caused by strong damping, that reduces resonance amplitudes.

The damping coefficient c_s decreases the first resonance, while c_0 decreases the second one. The influence of coefficients c_s and c_0 on resonance amplitudes is presented in Fig. 18, where κ is introduced as a damping decreasing factor according to the rule:

$$c_s^* = \frac{c_s}{\kappa}, \quad c_0^* = \frac{c_0}{3\kappa}. \tag{17}$$

Then, a new (decreased) damping coefficients c_s^* and c_s^* are used in simulations. Changing only c_s (c_0 is constant) according to Eq. (17), the first resonance can be observed, while the second one is small (Fig. 19). Note, that increasing c_s/c_s^* means low damping and vice versa. Thus, with decreasing damping c_s the second resonance appear while with strong damping only one resonance is visible (1.5 kHz). Two system resonances are better pronounced when c_s^* and c_0^* are introduced simultaneously (see Fig. 18). Notice that the energy dissipated by the MRE in the smartPFMT, measured by the energy loss factor (EL), shows an unexpected drop before the maximum peak occurring at the main resonance (Fig. 20). This behavior has also been observed in the 1dof MRE system (Fig. 14b), but in the linear scale it has not been visible.

The external excitation represented by voltage causes typical result, that is an increase of voltage generates stronger vibration of all system coordinates as shown in Fig. 21. The most important property of the resonance curves is that they are very similar to those of linear systems, without any significant symptoms of nonlinearity (e.g., no major hardening/softening behavior is observed), contrary to the case of 1dof MRE where nonlinearities together with hysteresis effect are revealed. This shows that smartPFMT can be used for the implantable middle ear hearing device without worrying about the development of irregular vibrations.

However, to show nonlinear phenomena in the smartPFMT system, next analyses are performed for $\kappa = 4$ and strong excitation $U = 4$ V and $U = 12$ V, that generate more complicated and interesting phenomena. First of all, $\kappa = 4$ reveals two resonances both for $U = 4$ V (Fig. 22a) and $U = 12$ V (Fig. 22b), that are strongly sensitive on the current (I). Increasing I the resonance peaks are moved left or right. Interestingly, this increase or decrease of resonance peak frequency seem to be chaotic, i.e. it is difficult to find relationships between resonance (shift and amplitude) and current (I) or voltage (U). The case when $I = 0$ A is the most interesting especially near $\omega = 500$–700 Hz, that is presented in bifurcation diagrams for $U = 4$ V and $U = 12$ V (Fig. 23). Especially for $U = 12$ V, the system is sensitive to initial conditions because vibration (solution) is different during the increasing and decreasing bifurcation parameter (ω). Moreover, the effect of bistability is observed for $\omega > 1$ kHz.

Without no doubt, voltage (U) is a key factor causing chaos and also bistability in the system. Fixing excitation frequency $\omega = 650$ Hz, two periodic solutions are visible for $U < 2$ V (Fig. 24a). Next, for 2 V $< U < 3$ V and $U > 7.8$ V chaotic vibration coexists with periodic one. Between 3 and 7.8 V, on the other hand the smartPFMT is unstable and exhibits multiple chaotic behavior. A basin of attraction performed for $\omega = 650$ Hz and $\omega = 12$ V is shown in Fig. 24b. A white region represents initial conditions (x_{s0} and v_{s0}) of harmonic vibrations, while the red one shows conditions of chaos. The basin is like ‘fractal island’. Examples of chaotic and harmonic vibration are depicted in Fig. 25a-b as time series and attractor on phase space with Poincaré points. Hysteresis loops of one period for the same cases are presented in Fig. 26. In case of chaos (Fig. 26a) the hysteresis loop is open and crossed.

Energy loss factor (EL) could be a good chaos indicator (Fig. 27). Generally, the most EL is near resonances.

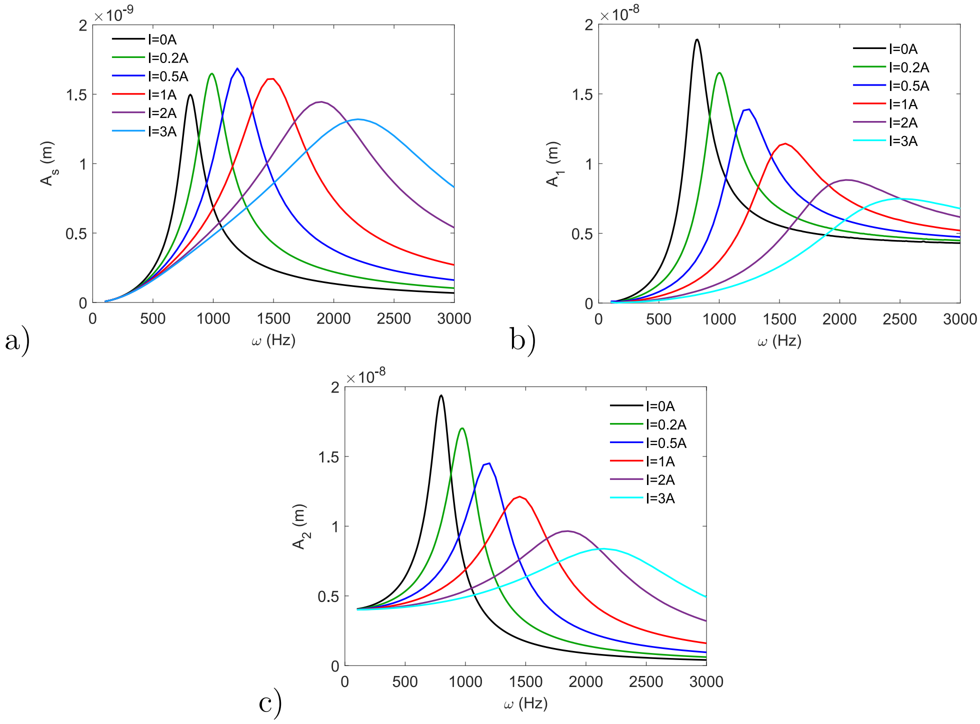

Fig. 17. Resonance curves of nonlinear system excited by smartPFMT (a), and left (b) and right (c) end of the PFMT versus excitation frequency for different current I.

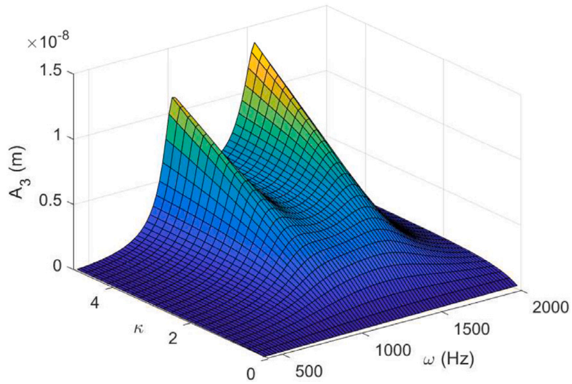

Fig. 18. Influence of damping decreasing factor (κ) on resonance curves of nonlinear system excited by smartPFMT at $I = 1$ A.

5. General application of smartPFMT

The smartPFMT can also be used in applications beyond micro-mechatronic systems; therefore, a larger actuator with mass $M_a = 10$ g is studied here. The parameters of the main system are as follows: $M_s = 54.78$ g, $k_s = 21.626$ N/m, $c_s = 19.098$ N s/m. Consequently, the natural frequency of the isolated main system is 124.78 Hz ($\sqrt{k_s/M_s}$). However, the main resonance of the system with the smartPFMT is 26 Hz at $I = 0$ A and increases with the current (I), as shown in Fig. 28, which presents a family of resonance curves for various voltage excitations. Moreover, as expected, the amplitudes increase with voltage (Fig. 28). Interestingly, the equivalent Young's modulus (EYM) depends on frequency and current, but not on voltage, which serves as an external excitation in this system (Fig. 29). The minimum of the EYM occurs exactly at the resonance frequency, whereas the energy loss (EL) curves (Fig. 30) peak at the resonance frequency and increase with voltage. Thus, the system excited using the smartPFMT demonstrates regular behavior under the assumed parameters. Interestingly, the hysteresis loop may have either a right- or left-sided slope, depending on the excitation frequency (ω) relative to the resonance frequency (ω_1). This means that if $\omega < \omega_1$, the hysteresis loop has a rightward slope, whereas if $\omega > \omega_1$, the slope is leftward (Fig. 31).

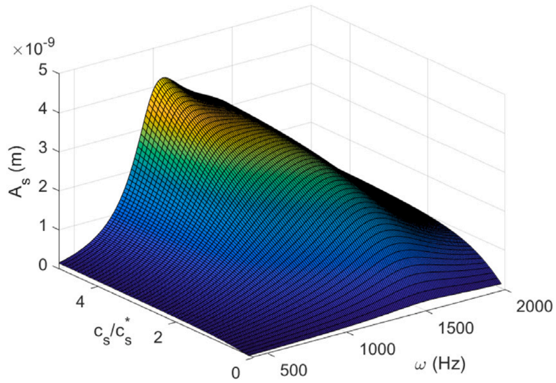

Fig. 19. Influence of damping coefficient c_s^* ($\kappa = c_s/c_s^*$)at c_0 = constant on resonance curves of nonlinear system excited by smartPFMT at $I = 1$ A.

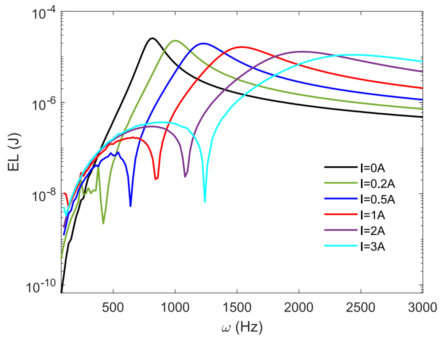

Fig. 20. Influence of charge (I) on energy loss for middle ear application of smartPFMT.

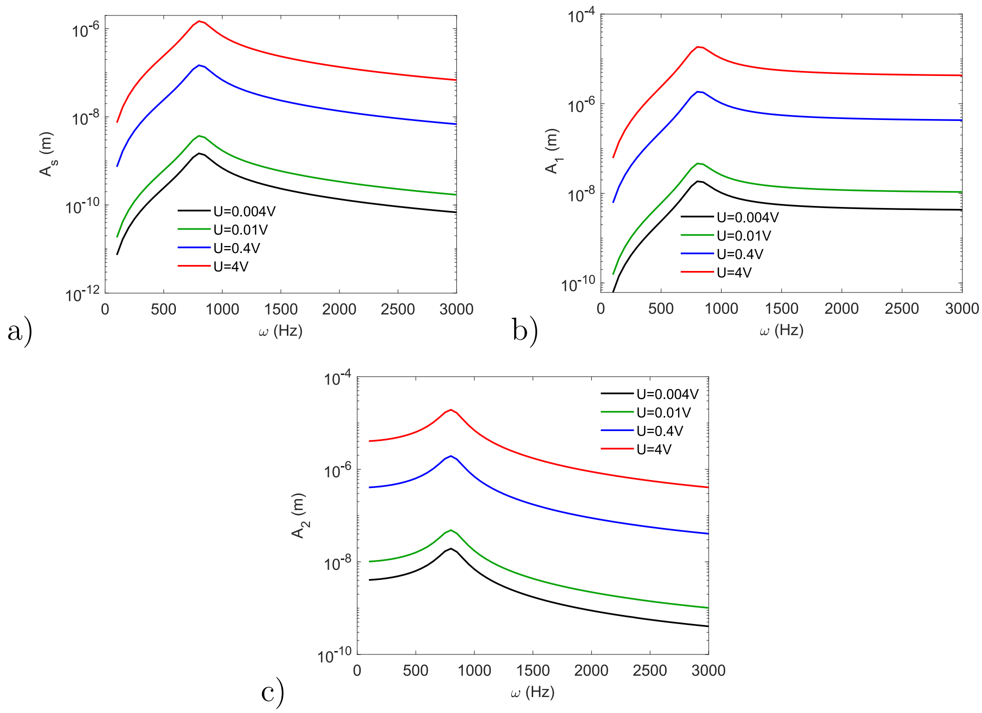

Fig. 21. Resonance curves of system excited by smartPFMT for different voltage U. Panel (a) represents M_s, (b) the left and (c) the right end of the smartPFMT.

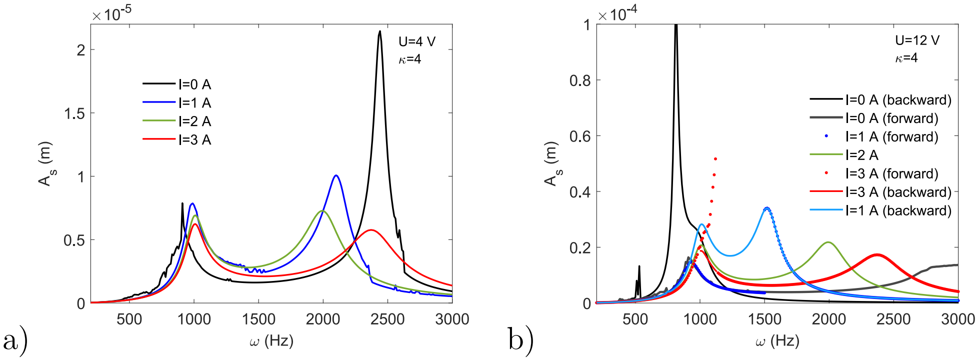

Fig. 22. Resonance curves of system excited by smartPFMT for $\kappa = 4$ and excitation $U = 4$ V (a), $U = 12$ V (b).

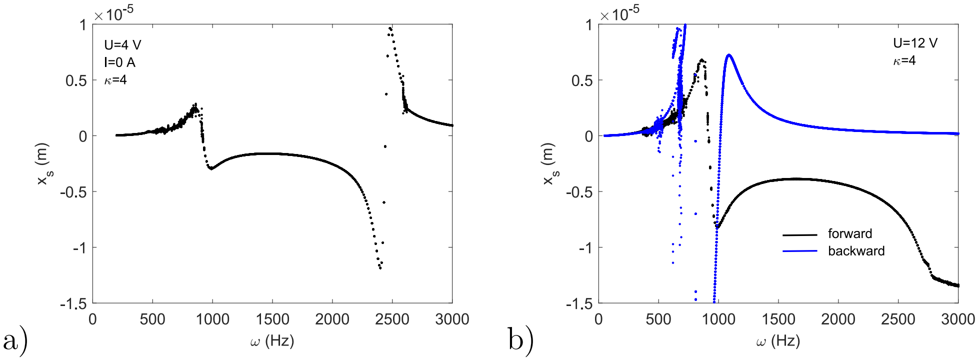

Fig. 23. Bifurcation diagrams of system excited by smartPFMT for $I = 0$, $\kappa = 4$ and $U = 4$ V (a), $U = 12$ V (b).

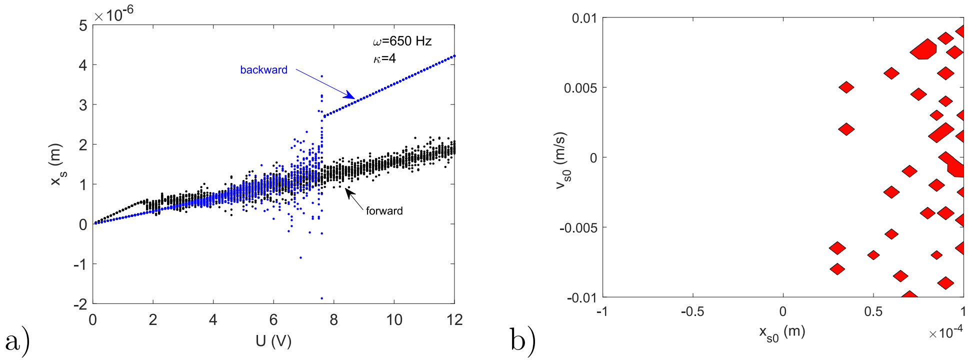

Fig. 24. Bifurcation diagram of m_s versus voltage (U) for $\omega = 650$ Hz and $\kappa = 4$ (a). Basin of attraction of m_s vibration for $U = 12$ V versus x_{s0} and v_{s0} (b).

The regular dynamic behavior observed in this case is due to the high damping coefficient of the main system (c_s). When c_s is small, quasi-periodic motion can occur, which disappears at $c_s = 0.005$ N s/m (Fig. 32a). Interestingly, the amplitude of the main mass (A_s) increases with the damping coefficient c_s (black, upper curve), while it remains nearly constant as c_s decreases (blue, lower curve). Consequently, two regular solutions are observed, indicating a bistability effect (Fig. 32b). For the lower branch (blue), the hysteresis loop has a leftward slope, whereas for the upper one, it is rightward (Fig. 33)—but only beyond the extrema of EYM and EL (Fig. 34). Before the extrema, the hysteresis loop has a leftward slope. This implies that the vibration amplitude, rather than the excitation frequency, determines the hysteresis loop slope. Thus, the behavior of the smartPFMT in general applications is typical and predictable, especially under strong damping. Systems with low damping can become unpredictable, particularly as damping increases.

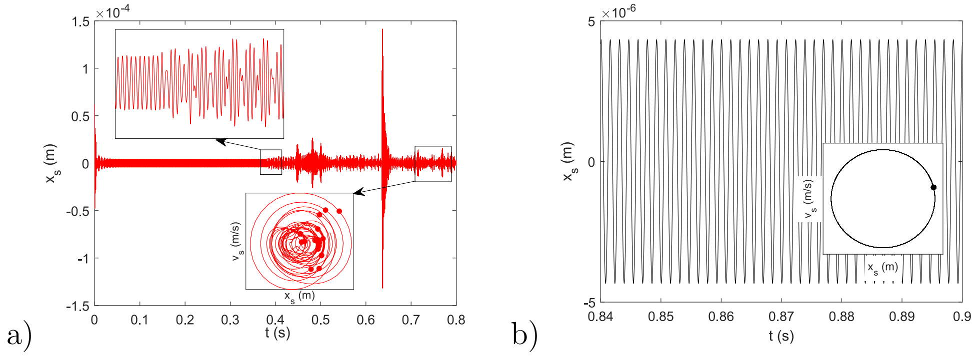

Fig. 25. Time series and attractor on phase space with Poincaré points of system excited by smartPFMT for $\kappa = 4$ and excitation $U = 12$ V, $\omega = 650$ Hz. Chaotic (a) and harmonic vibration (b). (For interpretation of the references to color in this figure, the reader is referred to the web version of this article.)

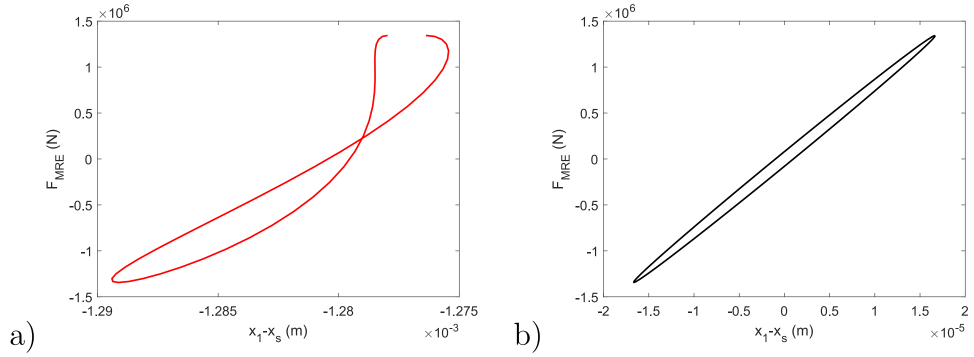

Fig. 26. Hysteresis loops of system excited by smartPFMT for $\kappa = 4$ and excitation $U = 12$ V, $\omega = 650$ Hz. Chaotic (a) and harmonic case (b).

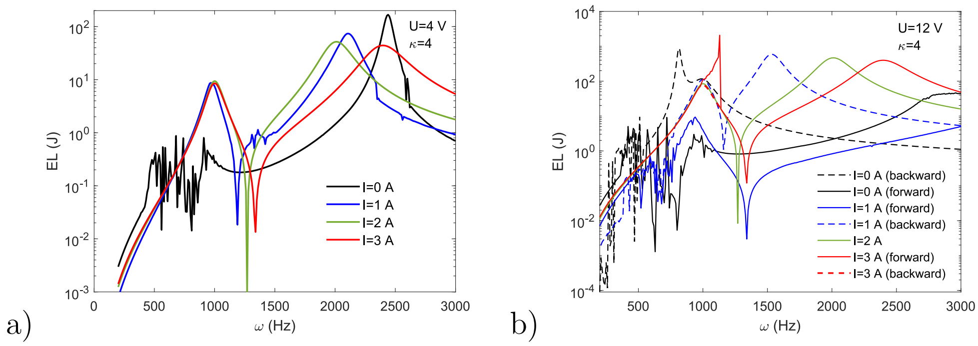

Fig. 27. Energy loss factor (EL) of system excited by smartPFMT for $\kappa = 4$, different current (I) and excitation $U = 4$ V (a), $U = 12$ V (b).

6. Discussion and conclusions

This study examines the application of a Piezoelectric Floating Mass Transducer (FMT) combined with a Magnetorheological Elastomer (MRE) for exciting the ossicular chain and general mechanical systems. The findings demonstrate that the FMT-MRE system effectively induces vibrations in the ossicular chain, suggesting its potential utility in hearing restoration and others medical and mechanical applications. The frequency response analysis indicates that resonance tuning and the adaptive mechanical properties of the MRE play a crucial role in optimizing performance. The piezoelectric material's use confirms its capability to generate sufficient vibratory motion. The MRE further enhances this attractiveness by providing tunable stiffness and damping properties, allowing for controlled vibration transmission. This variability was demonstrated through numerical experiment that showed the resonance frequency could be shifted by altering the electric current (I) applied to the MRE, ranging from 975 Hz at 0 A to 2670 Hz at 2 A. The accompanying decrease in vibration amplitude with increasing current highlights the system's strong damping effect, which is essential for reducing unwanted irregular vibration in practical applications such as middle ear implants.

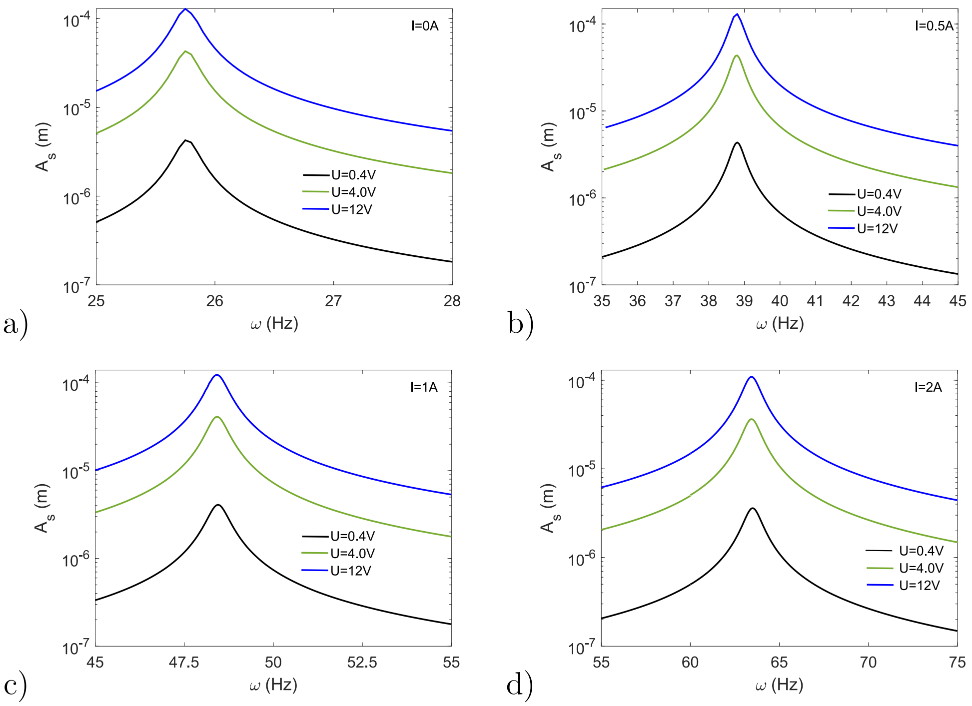

Fig. 28. Family of resonance curves of main system (A_s), in case of general application, excited by smartPFMT for various U and $I = 0$ A (a), $I = 0.5$ A (b), $I = 1$ A (c), $I = 2$ A (d).

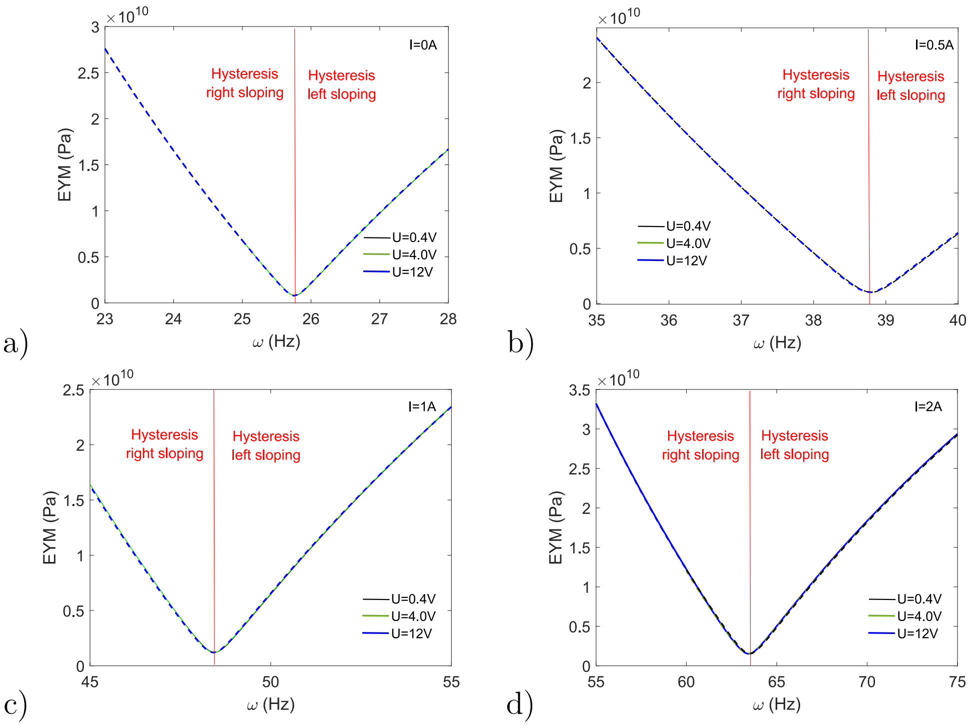

Fig. 29. Equivalent Young modulus (EYM) versus excitation frequency (ω) excited by smartPFMT for various voltage excitation (U) and electric current: $I = 0$ A (a), $I = 0.5$ (b), $I = 1$ A (c), $I = 2$ A (d).

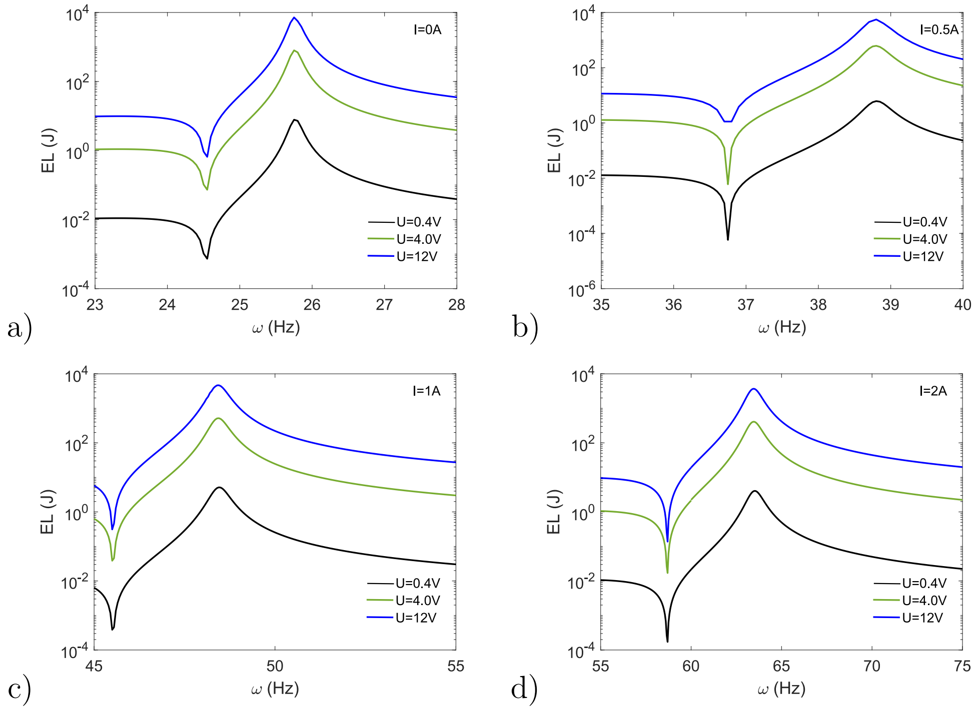

Fig. 30. Energy loss ratio (EL) versus excitation frequency (ω) excited by smartPFMT for various voltage excitation (U) and electric current: I = 0 A (a), I = 0.5 (b), I = 1 A (c), I = 2 A (d).

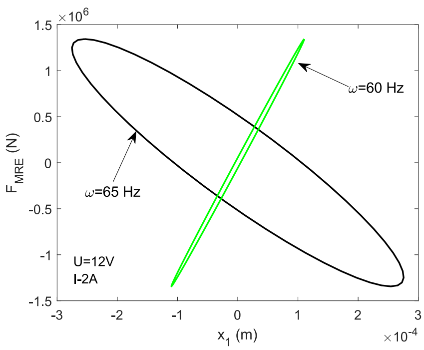

Fig. 31. Hysteresis loop for I = 2 A, U = 12 V and excitation frequency (a) ω = 60 Hz - before resonance; (b) ω = 65 Hz - after resonance.

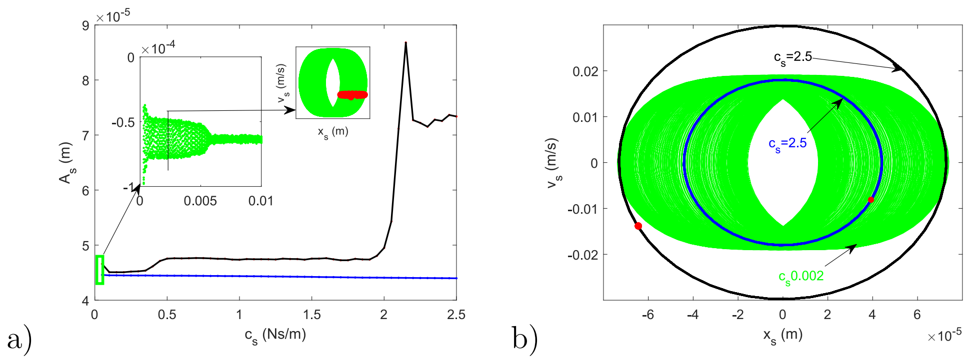

Fig. 32. Bifurcation diagram (a) and phase space diagrams (b) for U = 12 V, I = 2 A and various damping c_s. (For interpretation of the references to color in this figure, the reader is referred to the web version of this article.)

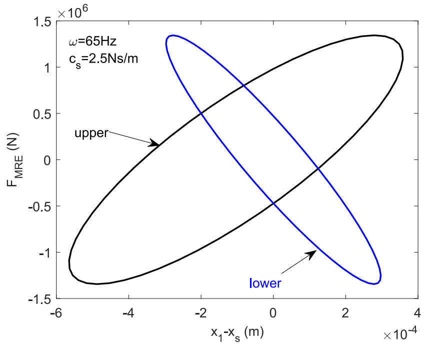

Fig. 33. Hysteresis loops for lower and upper solutions at $I = 2$ A, $U = 12$ V, $\omega = 65$ Hz.

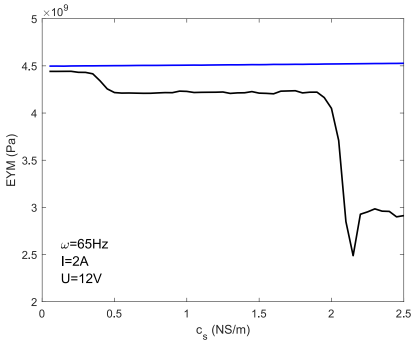

a)

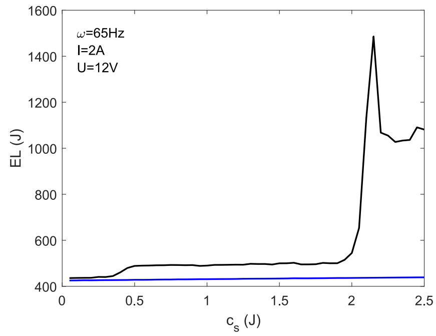

b)

Fig. 34. Equivalent Young modulus - EYM (a) and energy loss ratio - EL (b) versus damping c_s for $U = 12$ V and $I = 2$ A.

The pure hysteresis effect in 1dof MRE system was also analyzed in both low- and high-frequency regimes, confirming that as current is increased, the storage modulus rises while the loss modulus decreases. This indicates that the system becomes stiffer and dissipates less energy. However, it was observed that with stronger excitation amplitudes, the loss modulus increases, leading to higher energy loss. This trade-off between stiffness and energy loss needs careful management, especially in biomedical applications like middle ear implants, where energy efficiency is critical.

The smartPFMT offers a versatile solution for a variety of applications. Its adjustable resonance frequency, controlled by an electric current, allows it to be adapted to larger systems. In particular, the smartPFMT can be applied in broader engineering fields, including vibration control systems, energy harvesting devices, and dynamic systems requiring adaptable stiffness and damping. Compared to conventional actuators, the piezoelectric FMT combined with MRE demonstrates advantages in terms of size, adaptability, and energy efficiency. However, certain limitations, such as nonlinearities in response, bistability and dependency on external driving conditions, require further investigation. Nevertheless, classical electromagnetic FMTs sold commercially and implanted in the middle ear [21,46] also show a number of instabilities presented in the literature [22,49,50]. Nonlinear and unexpected behaviors can be eliminated by appropriate selection of device operating parameters and control system.

Finally, some conclusions can be drawn:

- The smartFMT, with its magnetorheological elastomer, successfully demonstrated variable resonance frequencies, offering flexibility for use in different mechanical systems, including hearing devices. This ability to adjust the resonance through electric current is a novel feature that enhances the device's adaptability.
- The system's damping properties, enhanced by the current-dependent MRE, help to reduce unwanted vibrations, making it an effective solution for middle ear implants where precise control of mechanical motion is essential. However, a balance must be maintained between increasing stiffness and minimizing energy loss, particularly under strong excitation.
- Dual Functionality: The smartFMT's ability to function as both an actuator and an energy harvester is a significant advantage, particularly in applications requiring efficient energy use, such as in medical implants. This dual functionality provides a sustainable solution for devices that need to operate with minimal external power input.
- The findings from this study open up new possibilities for the application of smartFMTs in medical and engineering fields, particularly in areas requiring precise control over mechanical vibrations and energy efficiency. Further research could explore the integration of smartFMTs in larger systems, as well as their long-term performance in clinical applications.

Applications and future plans

Floating Mass Transducers (FMTs), initially developed for auditory implants, have demonstrated significant versatility as compact, broadband vibration actuators and even energy harvesters. This contribution has enabled the integration of adaptive materials such as magnetorheological elastomers (MREs) into FMT structures, unlocking novel engineering applications where controllability, adaptability, and compact actuation are essential. Interesting properties of the FMT with MRE opens up a spectrum of applications in vibration control and adaptive structural systems.

In structural health monitoring and active vibration control, an FMT with MRE-based suspension could be embedded into lightweight civil or aerospace structures. By adjusting the mechanical coupling between the transducer and the host structure via magnetic field modulation, the system can adapt to changing operational conditions, such as load variations or environmental disturbances. This dynamic adaptability is particularly valuable in precision applications — e.g., satellite structures, drone systems, or turbine blades — where vibration profiles can be unpredictable and detrimental to performance or safety.

Similarly, in energy harvesting applications, an FMT-MRE system allows for real-time tuning of resonant conditions to optimize energy conversion efficiency. Ambient vibration sources often vary in frequency and amplitude. A tunable FMT, whose mechanical resonance can be shifted through the MRE's field-dependent stiffness, enables maximum power extraction under varying excitation conditions. This is particularly advantageous in environments with wideband or nonstationary vibrations, such as on rotating machinery, railway systems, or bridge structures.

The general advantages of using FMTs with MREs in engineering practice include:

1. Tunable dynamics where the system's natural frequency and damping can be actively modulated, improving the actuator's or harvester's bandwidth and adaptability to variable conditions.
2. Multi-functionality - the combination of actuation, sensing, and energy harvesting in a single device platform enables multifunctional nodes in smart systems (e.g., wireless sensor networks with self-powered actuation capability).
3. Magnetically controllable response without mechanical contact or moving parts. Control is achieved via an external magnetic field, reducing mechanical complexity and enhancing reliability.

In conclusion, the integration of magnetorheological elastomers into floating mass transducers extends their functional range beyond biomedical uses into engineering applications requiring real-time adaptability and resilience.

Future research should focus on optimal MRE material formulations, efficient magnetic control schemes, and co-design of FMT-MRE systems for specific engineering domains. Another important development consists of performing experiments, to validate the findings of the present paper. They will be focused on the dynamical phenomena highlighted in this work, that thus constitutes a necessary pre-requisite for the experimental part that is planned to be done in the future.

CRediT authorship contribution statement

R. Rusinek: Writing – original draft, Visualization, Software, Project administration, Methodology, Investigation, Funding acquisition, Formal analysis, Data curation, Conceptualization. **S. Lenci:** Writing – review & editing, Validation, Formal analysis.

Funding

This research was funded by the National Science Centre - Poland grant number UMO-2024/53/B/ST8/03778: The human ear dynamics stimulated by piezoelectric membrane - novel hybrid model.

Declaration of competing interest

The authors declare that they have no known competing financial interests or personal relationships that could have appeared to influence the work reported in this paper.

Data availability

Data will be made available on request.

References

[1] A. Arnold, M. Kompis, C. Candreia, F. Pfiffner, R. Häusler, C. Stieger, The floating mass transducer at the round window: Direct transmission or bone conduction? Hear. Res. 263 (1–2) (2010) 120–127, http://dx.doi.org/10.1016/j.heares.2009.12.019.
[2] T.M. Eßinger, M. Koch, M. Bornitz, N. Lasurashvili, M. Neudert, T. Zahnert, Sensor-actuator component for a floating mass transducer-based fully implantable hearing aid, Hear. Res. 378 (10) (2019) 157–165, http://dx.doi.org/10.1016/j.heares.2019.03.006.
[3] J. Maw, The vibrant soundbridge, Otolaryngol. Clin. North Am. 52 (2) (2019) 285–295, http://dx.doi.org/10.1016/j.otc.2018.11.007.
[4] H. Liu, J. Cheng, J. Yang, Z. Rao, G. Cheng, S. Yang, X. Huang, M. Wang, Concept and evaluation of a new piezoelectric transducer for an implantable middle ear hearing device, Sensors 17 (11) (2017) 2515, http://dx.doi.org/10.3390/s17112515.
[5] S. Busch, T. Lenarz, H. Maier, Comparison of alternative coupling methods of the vibrant soundbridge floating mass transducer, Audiol. Neurotol. 21 (6) (2017) 347–355, http://dx.doi.org/10.1159/000453354.
[6] M. Tisch, Implantable hearing devices, GMS Curr. Top. Otorhinolaryngol. - Head Neck Surg. 16 (2017) 1–22.
[7] R.M. Banakis Hartl, H.A. Jenkins, Implantable hearing aids: Where are we in 2020? Laryngoscope Investig. Otolaryngol. 5 (6) (2020) 1184–1191, http://dx.doi.org/10.1002/lio2.495.
[8] D. Beutner, K.-B. Hüttenbrink, Passive and active middle ear implants, GMS Curr. Top. Otorhinolaryngol. - Head Neck Surg. 8 (2009).

[9] D.S. Haynes, J.A. Young, G.B. Wanna, M.E. Glasscock, Middle ear implantable hearing devices: An overview, Trends Amplif. 13 (3) (2009) 206–214, http://dx.doi.org/10.1177/1084713809346262.

[10] S. Pelosi, M.L. Carlson, M.E. Glasscock, Implantable hearing devices, Otolaryngol. Clin. North Am. 47 (6) (2014) 953–965, http://dx.doi.org/10.1016/j.otc.2014.08.003.

[11] M.D. Seidman, T.A. Janz, J.A. Shohet, Totally implantable active middle ear implants, Otolaryngol. Clin. North Am. 52 (2) (2019) 297–309, http://dx.doi.org/10.1016/j.otc.2018.11.011.

[12] R.M. Rhodes, B.S. Tsai Do, Future of implantable auditory devices, Otolaryngol. Clin. North Am. 52 (2) (2019) 363–378, http://dx.doi.org/10.1016/j.otc.2018.11.017.

[13] R. Rusinek, K. Kecik, Effect of linear electromechanical coupling in nonlinear implanted human middle ear, Mech. Syst. Signal Process. 151 (1–2) (2021) 107391, http://dx.doi.org/10.1016/j.ymssp.2020.107391.

[14] E.-P. Hong, M.-K. Kim, I.-Y. Park, S.-h. Lee, Y. Roh, J.-H. Cho, Vibration modeling and design of piezoelectric floating mass transducer for implantable middle ear hearing devices, IEICE Trans. Fundam. E90–A (8) (2007) 1620–1627, http://dx.doi.org/10.1093/ietfec/e90-a.8.1620.

[15] Z.G. Wang, E.W. Abel, R.P. Mills, Y. Liu, Assessment of multi-layer piezoelectric actuator technology for middle-ear implants, Mechatronics 12 (1) (2002) 3–17, http://dx.doi.org/10.1016/S0957-4158(00)00067-2.

[16] Liu, Zhao, Yang, Rao, The influence of piezoelectric transducer stimulating sites on the performance of implantable middle ear hearing devices: A numerical analysis, Micromachines 10 (11) (2019) 782, http://dx.doi.org/10.3390/mi10110782.

[17] D. Shin, J.-H. Cho, Piezoelectric actuator with frequency characteristics for a middle-ear implant, Sensors 18 (6) (2018) 1694, http://dx.doi.org/10.3390/s18061694.

[18] D.H. Shin, K.W. Seong, H.H. Nakajima, S. Puria, J.-H. Cho, A piezoelectric bellows round-window driver (PBRD) for middle-ear implants, IEEE Access 8 (2020) 137947–137954, http://dx.doi.org/10.1109/ACCESS.2020.3010539.

[19] I.-Y. Park, Y. Shimizu, K.N. O'Connor, S. Puria, J.-H. Cho, Comparisons of electromagnetic and piezoelectric floating-mass transducers in human cadaveric temporal bones, Hear. Res. 272 (1–2) (2011) 187–192, http://dx.doi.org/10.1016/j.heares.2010.10.17.

[20] E.-P. Hong, I.-Y. Park, K.-W. Seong, C.-W. Lee, M.-N. Kim, J.-H. Cho, Application of piezoelectric multi-layered actuator to floating mass transducer for implantable middle ear hearing devices, J. Electroceramics 23 (2–4) (2009) 335–340, http://dx.doi.org/10.1007/s10832-008-9451-0.

[21] A. Pegan, Active middle ear vibrant soundbridge sound implant, Acta Clin. Croat. (2019) http://dx.doi.org/10.20471/acc.2019.58.02.20.

[22] R. Rusinek, S. Lenci, Stapes vibrations induced by piezoelectric floating mass transducer, J. Sound Vib. 548 (11) (2023) 117556, http://dx.doi.org/10.1016/j.jsv.2023.117556.

[23] H.-J. Jung, S.-J. Lee, D.-D. Jang, I.-H. Kim, J.-H. Koo, F. Khan, Dynamic characterization of magneto-rheological elastomers in shear mode, IEEE Trans. Magn. 45 (10) (2009) 3930–3933, http://dx.doi.org/10.1109/TMAG.2009.2024886.

[24] Y. Shen, M.F. Golnaraghi, G.R. Heppler, Experimental research and modeling of magnetorheological elastomers, J. Intell. Mater. Syst. Struct. 15 (1) (2004) 27–35, http://dx.doi.org/10.1177/1045389X04039264.

[25] Z. Xu, Z. Tang, H. Wu, X. Bo, F. Chen, X. Wang, K. Chen, S. Jiang, G. Zhang, Study on the trajectory of magnetic particles in the process of magnetorheological elastomer pre-structure, J. Magn. Magn. Mater. 549 (4–5) (2022) 169014, http://dx.doi.org/10.1016/j.jmmm.2021.169014.

[26] W. Gao, Z. Guo, Y. Yang, Effect of intensity of orientational magnetic field on steady shear behavior of magnetorheological elastomers, AIP Adv. 11 (5) (2021) 055102, http://dx.doi.org/10.1063/5.0044202.

[27] A. Saber, R. Sedaghati, The modeling of magnetorheological elastomers: A state–of–the–art review, Adv. Eng. Mater. 67 (2023) 1167, http://dx.doi.org/10.1002/adem.202300182.

[28] F. Guo, C.-b. Du, R.-p. Li, Viscoelastic parameter model of magnetorheological elastomers based on abel dashpot, Adv. Mech. Eng. 6 (4) (2014) 629386, http://dx.doi.org/10.1155/2014/629386.

[29] J.-T. Zhu, Z.-D. Xu, Y.-Q. Guo, Magnetoviscoelasticity parametric model of an MR elastomer vibration mitigation device, Smart Mater. Struct. 21 (7) (2012) 075034, http://dx.doi.org/10.1088/0964-1726/21/7/075034.

[30] J.-T. Zhu, Z.-D. Xu, Y.-Q. Guo, Experimental and modeling study on magnetorheological elastomers with different matrices, J. Mater. Civ. Eng. 25 (11) (2013) 1762–1771, http://dx.doi.org/10.1061/(ASCE)MT.1943-5533.0000727.

[31] Z.D. Xu, Y.X. Liao, T. Ge, C. Xu, Experimental and theoretical study of viscoelastic dampers with different matrix rubbers, J. Eng. Mech. 142 (8) (2016) 143, http://dx.doi.org/10.1061/(ASCE)EM.1943-7889.0001101.

[32] T.A. Nadzharyan, V.V. Sorokin, G.V. Stepanov, A.N. Bogolyubov, E.Y. Kramarenko, A fractional calculus approach to modeling rheological behavior of soft magnetic elastomers, Polym. 92 (17) (2016) 179–188, http://dx.doi.org/10.1016/j.polymer.2016.03.075.

[33] F.-L. Xin, X.-X. Bai, L.-J. Qian, Modeling and experimental verification of frequency-, amplitude-, and magneto-dependent viscoelasticity of magnetorheological elastomers, Smart Mater. Struct. 25 (10) (2016) 105002, http://dx.doi.org/10.1088/0964-1726/25/10/105002.

[34] U.R. Poojary, K.V. Gangadharan, Integer and fractional order-based viscoelastic constitutive modeling to predict the frequency and magnetic field-induced properties of magnetorheological elastomer, J. Vib. Acoust. 140 (4) (2018) 129501, http://dx.doi.org/10.1115/1.4039242.

[35] J. Yang, H. Du, W. Li, Y. Li, J. Li, S. Sun, H.X. Deng, Experimental study and modeling of a novel magnetorheological elastomer isolator, Smart Mater. Struct. 22 (11) (2013) 117001, http://dx.doi.org/10.1088/0964-1726/22/11/117001.

[36] M. Behrooz, X. Wang, F. Gordaninejad, Performance of a new magnetorheological elastomer isolation system, Smart Mater. Struct. 23 (4) (2014) 045014, http://dx.doi.org/10.1088/0964-1726/23/4/045014.

[37] S.-H. Eem, H.-J. Jung, J.-H. Koo, Modeling of magneto-rheological elastomers for harmonic shear deformation, IEEE Trans. Magn. 48 (11) (2012) 3080–3083, http://dx.doi.org/10.1109/TMAG.2012.2205140.

[38] H. Vatandoost, M. Norouzi, S.M.S. Alehashem, S.K. Smoukov, A novel phenomenological model for dynamic behavior of magnetorheological elastomers in tension–compression mode, Smart Mater. Struct. 26 (6) (2017) 065011, http://dx.doi.org/10.1088/1361-665X/aa6126.

[39] M. Ismail, F. Ikhouane, J. Rodellar, The hysteresis Bouc-Wen model, a survey, Arch. Comput. Methods Eng. 16 (2) (2009) 161–188, http://dx.doi.org/10.1007/s11831-009-9031-8.

[40] A. Hall, M. Allahverdi, E.K. Akdogan, A. Safari, Development and electromechanical properties of multimaterial piezoelectric and electrostrictive PMN-PT monomorph actuators, J. Electroceramics 15 (2) (2005) 143–150, http://dx.doi.org/10.1007/s10832-005-2191-5.

[41] G. Sebald, L. Lebrun, D. Guyomar, Modeling of elastic nonlinearities in ferroelectric materials including nonlinear losses: Application to nonlinear resonance mode of relaxors single crystals, IEEE Trans. Ultrason. Ferroelectr. Frequency Control. 52 (4) (2005) 596–603, http://dx.doi.org/10.1109/TUFFC.2005.1428042.

[42] Q. Guo, G.Z. Cao, I.Y. Shen, Measurements of piezoelectric coefficient d33 of lead zirconate titanate thin films using a mini force hammer, J. Vib. Acoust. 135 (1) (2013) 011003, http://dx.doi.org/10.1115/1.4006881, arXiv:https://asmedigitalcollection.asme.org/vibrationacoustics/article-pdf/135/1/011003/6338675/vib_135_1_011003.pdf.

[43] S. Ramesh, D. Ravinder, K.C.B. Naidu, Nagasamudram, S. Kumar, K. Srinivas, D.B. Basha, B.C. Sekhar, A review on giant piezoelectric coefficient, materials and applications, Biointerface Res. Appl. Chem. 9 (5) (2019) 4205–4216, http://dx.doi.org/10.33263/BRIAC95.205216.

[44] P. Shivashankar, S. Gopalakrishnan, S. Kandagal, Nonlinear modeling of d33-mode piezoelectric actuators using experimental vibration analysis, J. Sound Vib. 505 (2021) 116151, http://dx.doi.org/10.1016/j.jsv.2021.116151, URL https://www.sciencedirect.com/science/article/pii/S0022460X21002236.

[45] T. Chen, L.-J. Ren, D.-M. Yin, J. Li, L. Yang, P.-D. Dai, T.-Y. Zhang, A comparative study of MED-EL FMT attachment to the long process of the incus in intact middle ears and its attachment to disarticulated stapes head, Hear. Res. 353 (2017) 97–103, http://dx.doi.org/10.1016/j.heares.2017.06.006.
[46] J.J. Rosowski, W. Chien, M.E. Ravicz, S.N. Merchant, Testing a method for quantifying the output of implantable middle ear hearing devices, Audiol. Neuro-Otol. 12 (4) (2007) 265–276, http://dx.doi.org/10.1159/000101474.
[47] N. Gao, Y.Z. Chen, F.L. Chi, T.Y. Zhang, H.D. Xu, H.Y. Kang, T.Z. Pan, The frequency response of a floating piezoelectric microphone for the implantable middle ear microphone, Laryngoscope 123 (6) (2013) 1506–1513, http://dx.doi.org/10.1002/lary.23618.
[48] R. Rusinek, M. Szymanski, R. Zablotni, Biomechanics of the human middle ear with viscoelasticity of the maxwell and the Kelvin–Voigt type and relaxation effect, Mater. 13 (17) (2020) 3779, http://dx.doi.org/10.3390/ma13173779.
[49] A. Weremczuk, R. Rusinek, Dynamics of the middle ear with an implantable hearing device: An improved electromechanical model, Nonlinear Dyn. 112 (3) (2024) 2219–2235, http://dx.doi.org/10.1007/s11071-023-09141-y.
[50] H. Liu, Z. Liu, J. Liu, T. Lenarz, H. Maier, Effect of electromagnetic transducer design parameters on round-window stimulation in otosclerosis: A nonlinear dynamic analysis, Nonlinear Dyn. 113 (14) (2025) 18727–18744, http://dx.doi.org/10.1007/s11071-025-11149-5.